

Electronic Characteristics and Charge Transport Mechanisms for Large Area Aromatic Molecular Junctions

Adam Johan Bergren,^{*,†} Richard L. McCreery,^{†,‡} Stanislav R. Stoyanov,[†] Sergey Gusarov,[†] and Andriy Kovalenko^{†,§}

National Institute for Nanotechnology, National Research Council Canada, Edmonton, Alberta, Canada, Department of Chemistry, University of Alberta, Edmonton, Alberta, Canada, and Department of Mechanical Engineering, University of Alberta, Edmonton, Alberta, Canada

Received: July 9, 2010; Revised Manuscript Received: August 12, 2010

This paper reports the electron transport characteristics of carbon/molecule/Cu molecular junctions, where aromatic molecules (azobenzene or AB and nitroazobenzene or NAB) are employed as the molecular component. It is shown that these devices can be made with high yield (>90%), display excellent reproducibility, and can withstand at least 1.5×10^9 potential cycles and temperatures of at least 180 °C. Transport mechanisms are investigated by analysis of current density/voltage (J – V) curves as a function of the molecular layer thickness and temperature. Results show that J decreases exponentially with thickness, giving a measured value for the low-bias attenuation factor (β) of $2.5 \pm 0.1 \text{ nm}^{-1}$ for AB and NAB. In addition, it is shown that transport is not thermally activated over a wide range of temperatures (5–450 K) and that the appearance of a thermally “activated” region at higher temperatures can be accounted for by the effect of temperature on the distribution of electrons around the Fermi level of the contact(s). These results indicate that quantum mechanical tunneling is likely the mechanism for charge transport in these junctions. Although application of the Simmons tunneling model leads to transport parameters consistent with nonresonant tunneling, the parameters obtained from fitting experimental data indicate that the barrier height and/or shape, effective mass, and dielectric constant (ϵ) can all change with thickness. Experimental measurements of ϵ and density functional theory (DFT) calculations of molecular energy levels and polarizability support these conclusions. Finally, the implications of the transport mechanisms are discussed from the viewpoint of designing functional molecular electronic devices.

1. Introduction

Molecular electronics has been an active area of research motivated by a variety of potential applications.^{1–8} Often researchers seek to utilize the wide variety of molecular energy levels encountered in organic structures to augment the function of existing microelectronic devices. To this end, the transport of electronic charge through organic moieties has been measured using a variety of formats and techniques,⁴ both at the single molecule level⁶ and for junctions containing large ensembles of molecules.^{9–15} In the latter case, a typical device is made by starting with a molecular layer adsorbed onto a conducting (or semiconducting) surface and then applying top contact materials. The current/voltage behavior of molecular junctions with varying structure and thickness is compared with theoretical predictions to elucidate the mechanism(s) of electron transport.¹⁴ Moreover, predictions of these models with the variation of parameters such as molecular structure, junction thickness, bias voltage, and temperature are used to confirm proposed mechanisms.

Our group fabricates electronic junctions by vapor-depositing metallic top contacts onto 1–6 nm thick molecular ensembles chemisorbed on flat (rms roughness < 0.5 nm) carbon surfaces by reduction of aromatic diazonium reagents.¹⁶ This procedure leads to the formation of an aromatic molecular layer of

controllable thickness¹⁷ that is anchored by a carbon–carbon covalent bond with the long molecular axis approximately perpendicular to the substrate surface. The use of carbon as a bottom contact results in the formation of a symmetric, conjugated phenyl–phenyl bond such that there is likely to be strong electronic coupling between the molecule and the carbon substrate, as well as a weak interfacial dipole. Furthermore, this method is capable of a very high yield and excellent reproducibility¹³ compared to many alternative approaches. Finally, the junction structure is amenable to integration into commercial microelectronic processing due to its robust nature and thermal stability. Diazonium-derived molecular layers have been characterized using Raman,^{18,19} infrared,²⁰ UV–vis,²¹ XPS,^{18,22} AFM,^{17,23,24} and other techniques.²⁵ These studies have shown that the layers are oriented, densely packed, and thermally and chemically stable in a wide range of conditions. Infrared characterization²⁰ showed an average 30° tilt of the molecular axis from the surface normal, even for multilayer films. Thus, a general picture of the junction structure consists of a smooth carbon conductor with a covalently bonded, partially disordered (but oriented) molecular layer, 1–5 molecules thick, with a metallic top contact. A schematic of the junction structure is shown in Scheme 1.

In this paper we investigate charge transport mechanisms in carbon-based molecular junctions by characterizing the electronic characteristics of molecular junctions containing varying thicknesses of AB and NAB over a wide range of temperatures (5–450 K). The dependence of the J – V curves on thickness

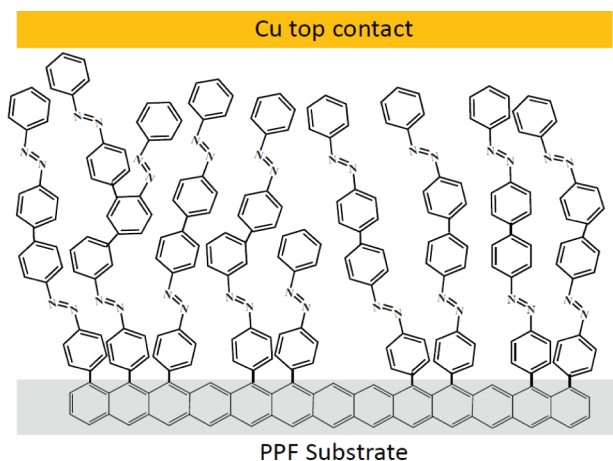
* To whom correspondence should be addressed. E-mail: adam.bergren@nrc.ca.

[†] National Research Council Canada.

[‡] Department of Chemistry, University of Alberta.

[§] Department of Mechanical Engineering, University of Alberta.

SCHEME 1: Structure of an AB Molecular Junction Used in This Work That Is Consistent with the Numerous Characterizations Carried out on These Structures^a



^a Molecular layer thickness can be controlled by deposition parameters and is verified with AFM.

and temperature are analyzed in the context of the nonresonant Simmons tunneling model and the possibility of resonant transport contributing to the current is also discussed. The results indicate a pronounced difference in conduction behavior for aromatic molecular layers compared to more commonly studied aliphatic layers, and demonstrate nondissipative electron transport across 2–5 nm thick multilayers over a wide range of temperatures (5–450 K). The preference in the literature for aliphatic molecular layers in molecular electronic systems largely stems from the well-defined nature of molecular monolayers (e.g., alkanethiolates and related –SH containing molecules on Au); their high packing density and structural organization provide a convenient pathway to producing molecular layers with known thickness. However, aromatic molecular layers offer several advantages, including a wider range of possible energy levels and an increased number of possible molecular structures such that a wider range of electronic functions may be envisioned. Furthermore, the high reproducibility and temperature stability of carbon-based junctions reported here represent important first steps toward the integration of molecular electronic devices with conventional microelectronic circuits.

2. Experimental Section

The fabrication of carbon/molecule/Cu junctions was described in detail in a previous report,¹³ based on a carbon substrate consisting of a pyrolyzed photoresist film (PPF)²⁶ on thermally grown SiO₂ (~300 nm thickness) on Si. PPF is produced by the pyrolysis of commercially available photoresist, as described in detail elsewhere.²⁶ The pyrolysis procedure partially graphitizes the photoresist, resulting in a conductive carbon film that has a resistivity close to that of glassy carbon (~6 × 10⁻³ Ω cm for a 1 μm thick film).²⁶ PPF is flat on a molecular scale, with a roughness (<0.5 nm rms) similar to that of the substrate upon which it is made.

Molecular layers are deposited onto the carbon substrate by reduction of aromatic diazonium reagents. The carbon surface (PPF) is used as the working electrode in a three-electrode electrochemical cell in a dilute solution (1.0 mM) of diazonium precursor in acetonitrile (with 0.1 M tetrabutylammonium tetrafluoroborate as supporting electrolyte). A potential sweep

program is initiated from a potential where no reduction occurs (+0.4 V vs Ag/Ag⁺) to a negative voltage past the half wave potential for reduction of the diazonium salt (the observed half-wave potential of NAB diazonium salt is ≈ -0.2 V) at a sweep rate of 0.2 V s⁻¹. Thickness is controlled in the 2–6 nm range (corresponding to 1–4 molecular layers) by varying the cathodic switching potential from -0.4 to -0.6 V, and the total number of sweeps (for a -0.6 V switching potential) from 1 to 10. Thicknesses are always verified using an atomic force microscopy “scratching” method, as discussed elsewhere.¹⁷ It is important to emphasize that the molecular layers deposited in this way are multilayers.^{23,24} Growth of a second layer onto the first is still mediated by electroreduction, resulting in a surface polymerization reaction. If the conditions during growth are controlled carefully, very uniform, smooth (rms roughness similar to that for the PPF substrate), and pinhole-free adlayers result.^{23,27} Presumably, these conditions result in the preferential bonding of radicals to the underlying surface due to the faster rate of electroreduction at uncoated areas. Subsequent layers then bond to the initial layer at a slower rate, and growth continues until the rate of electroreduction is too slow to continue. If high precursor concentrations, excessively negative potentials, or long electrolysis times are used, thicker layers can be made, but their growth proceeds unevenly²⁴ and they are therefore not suitable for fabrication of molecular electronic junctions.

Junctions are designated from bottom to top with the molecular layer thickness in nm determined by AFM in parentheses, for example, PPF/NAB(4.5)/Cu. In all cases reported herein, the top contact was a 30 nm layer of Cu followed by a 15 nm layer of Au deposited by electron beam deposition at <1 × 10⁻⁵ Torr. Previous reports on PPF/molecule/Cu junctions^{12,13,28} have repeatedly demonstrated a high level of yield and reproducibility, as discussed below. A previous report also showed that copper oxides do not contribute to the electronic response of the system.¹³

A Janis ST-500-1 cryogenic probe station with liquid He or liquid N₂ cooling was used to collect *J*–*V* curves over a temperature range of 5–450 K, with the sample in a vacuum of ~10⁻⁶ Torr. *J*–*V* curves were acquired with a 4-wire geometry using a Labview-based data acquisition system. This system corrects for ohmic losses in both the bottom and top contacts. In all cases, a positive *V* indicates that the bottom carbon contact (PPF) is more positive than the Cu top contact. Positive current indicates electron transport from the Cu through the molecular layer to the PPF substrate.

3. Results and Discussion

3.1. Device Reproducibility and Cycle Life. Figure 1 shows overlays of eight *J*–*V* curves on linear (A and C) and semilogarithmic (B and D) scales for junctions containing two different molecules, azobenzene (AB, curves A and B) and nitroazobenzene (NAB, curves C and D). Responses from all eight junctions fabricated on a single chip are shown, to serve as an example of the excellent yield and reproducibility. For the AB junctions, the relative standard deviation (RSD) of *J* (linear values) is 9.3% at +0.1 V (i.e., *J* = 0.043 ± 0.004 Å cm⁻²) and 21% at +0.5 V (*J* = 1.4 ± 0.3 Å cm⁻²), while the NAB junctions have RSD values of 9.5 and 26% at +0.1 and +0.5 V, respectively. In both cases, the yield was 100% (8/8). In general, as reported recently,¹³ the yield of PPF/NAB(4.5)/Cu junctions is typically >90% if care is taken to reproduce the conditions during fabrication. In the current study, the overall yield for 72 junctions on nine chips (representing the five

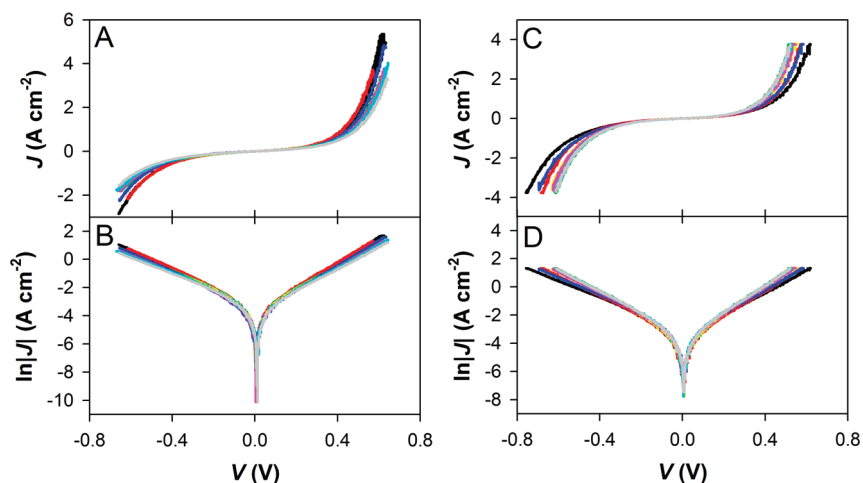


Figure 1. Overlay of J - V curves for 8 PPF/AB(3.5)/Cu junctions on a single chip for linear (A) and semilogarithmic (B) scales. The yield was 100% (8/8) and the relative standard deviation (RSD) of J for +0.1 V was 9.3% (i.e., $J = 0.043 \pm 0.004 \text{ \AA cm}^{-2}$) and for +0.5 V was 21% ($J = 1.4 \pm 0.3 \text{ \AA cm}^{-2}$). Same data set for 8 PPF/NAB(3.3)/Cu junctions on linear (C) and semilog (D) scales, where the RSD was 9.5 and 26% at +0.1 and +0.5 V, respectively.

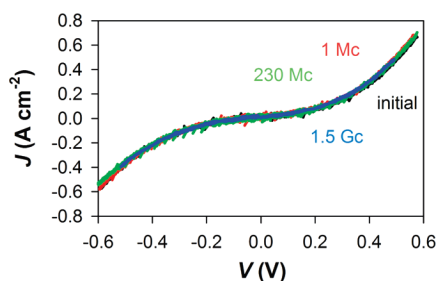


Figure 2. Triangle wave cycling of a single PPF/NAB(3.3)/Cu junction up to 1.5×10^9 cycles over the course of 90 h in lab ambient, during which a DC current of ± 1 mA passed through the device at the voltage amplitude maximum. Junction area = 0.0017 cm^2 .

different NAB thicknesses and four different AB thicknesses shown in Figure 3) was 95.8% (69/72), where the three nonworking devices displayed high, linear currents characteristic of direct PPF to Cu contact. The low incidence of short circuits from metal penetration indicates that the molecular layers are densely packed over their relatively large areas (0.0017 cm^2 or $\sim 10^{11}$ molecules).

To assess the impact of repeated voltage cycling on these devices, a single junction was scanned over 1.5×10^9 times, with J - V curves recorded at intervals. Figure 2 shows the J - V curves (on a linear scale to facilitate direct comparison) for a single PPF/NAB(3.3)/Cu junction recorded using a function generator and data acquisition system in a 3-wire mode (see Supporting Information for details). The initial curve (black) was recorded before initiating a 1 kHz triangle wave of ± 0.6 V amplitude for 17 min (1.02 Megacycles, or Mc, red curve). This waveform was then applied for an additional 64.5 h, yielding a total of 230 Mc (green curve). Finally, a 15 kHz wave was applied for 24 h, adding 1.3 Gc for a total of 1.5 Gc (blue curve). These relatively low frequencies were employed to ensure that the capacitance of the device (which becomes significant above ~ 20 kHz) did not obscure the DC current. The results in Figure 2, therefore, indicate that these devices survive the application of at least 1.5×10^9 cycles to voltages of >0.5 V, which yielded a current of ~ 1 mA ($\sim 0.6 \text{ A/cm}^2$) at peak applied voltage. Thus, Figures 1 and 2 demonstrate that PPF/molecule/Cu junctions fabricated using diazonium chemistry have reproducible J - V behavior, excellent yield, and are very robust to potential cycling. In addition, as shown in the

Supporting Information, these devices show only minimal changes in J - V curves after aging in air for 270 days (see Figure S-1 in the Supporting Information). As will be discussed below, these devices also survive temperatures of at least $180 \text{ }^\circ\text{C}$ in vacuum (where the temperature dependence of conductance was tested). The thermal and cycling stability of carbon/molecule/Cu junctions, as well as the ability to use vapor deposited top contacts, are necessary prerequisites for compatibility of molecular components with current commercial microelectronic processing and operation. We now consider the conduction mechanism in these devices through investigation of the thickness and temperature dependence of electron transport.

3.2. Evaluation of Distance Dependence of Transport.

Figure 3 shows the effect of thickness on the electrical properties of carbon/molecule/Cu junctions. Figure 3A shows J - V curves for PPF/AB/Cu junctions as a function of the thickness of AB in the range from 2–5 nm, while Figure 3B shows the corresponding plots for NAB. Analysis of these curves reveals several trends. First, in all cases, J increases linearly with V at low bias (see Figure S-2 in Supporting Information for plots with a linear J scale), while at higher bias J is an exponential function of V . Second, as illustrated by the attenuation plots in Figure 3C, junction conductance decreases exponentially as the molecular layer thickness (d) increases. The attenuation factor (β , the absolute value of the slope) determined from these plots is 2.51 and 2.47 nm^{-1} for AB and NAB, respectively (at low applied bias, see Supporting Information, Figure S-3, and discussion for the effect of voltage on β). These observations are consistent with previous measurements of PPF/molecule/Cu devices, where β values of $\sim 2.2 \text{ nm}^{-1}$ were reported for biphenyl and nitrophenyl junctions¹² and for electrochemical reactions at carbon electrodes modified with similar aromatic structures.²⁹ Finally, Figure 3D shows that the low voltage junction resistance (R_{1v}) increases exponentially with thickness. The values of β determined from this analysis (2.42 and 2.37 nm^{-1} for AB and NAB, respectively) are in good agreement with the values determined in Figure 3C. Although the plots in Figure 3C and 3D are expected to correlate because 0.1 V falls within the linear regime, they are both included because both formats are commonly reported in literature. In addition, the extrapolated contact resistance (R_c) values determined from the intercept of the plots in Figure 3D are $0.31 \text{ } \Omega$ ($3.7 \times 10^{-4} \text{ } \Omega \text{ cm}^2$) for AB and $0.38 \text{ } \Omega$ ($6.5 \times 10^{-4} \text{ } \Omega \text{ cm}^2$) for NAB. In both

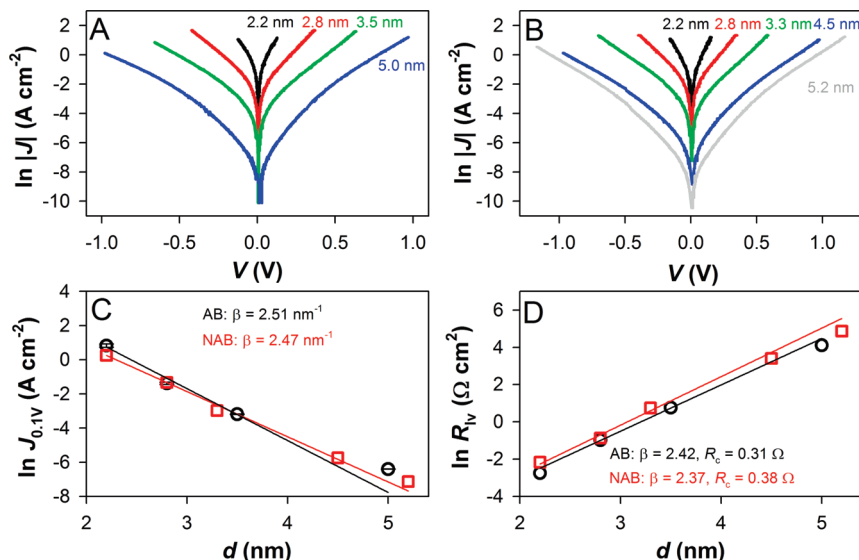


Figure 3. J - V curves for AB (A) and NAB (B) as a function of thickness. (C) Attenuation plots from the current density at +0.1 V, illustrating that J falls off exponentially with d , yielding β values of 2.51 and 2.47 nm^{-1} for AB and NAB, respectively. (D) Attenuation plots constructed from the low voltage resistance (i.e., the inverse slope of the linear portion of the J - V curve) yielding $\beta = 2.42 \text{ nm}^{-1}$ (AB) and 2.37 nm^{-1} (NAB) and $R_c = 0.31 \text{ } \Omega$ (AB) and $0.38 \text{ } \Omega$ (NAB).

cases, the value of R_c represents a negligible contribution to R_{IV} (e.g., the lowest R_{IV} value, which is for the 2.2 nm AB layer, is 53 Ω , illustrating that R_c is less than 0.6% of the lowest R_{IV} value and much less for thicker layers). Throughout the entire voltage range measured for all junctions, the value of R_c does not exceed 5% of the differential resistance values, illustrating that the electronic responses we observe are dominated by the resistance of the molecular component and not by contact resistance. In addition, the R_c values we obtain are lower than those often reported for alkanethiolate-based devices^{30,31} and imply relatively strong electronic coupling between the NAB and the contacts.³²

Because the shape of the J - V curves and the exponential thickness dependence are consistent with a quantum mechanical tunneling mechanism, we have measured the temperature-dependent conductance to further narrow the possible conduction mechanism in these devices. Tunneling is known to be a temperature-independent process, while many other conduction mechanisms have at least a weak, and in many cases, a strong dependence of the current density on temperature.

3.3. Temperature Dependence of Transport. Figure 4A shows a series of J - V curves for a PPF/AB(3.2)/Cu junction taken over a range of temperatures from 9 to 450 K. Two distinct regions are observed, a temperature-independent region below ~ 250 K and a slightly temperature dependent response at more elevated temperatures. The changes with temperature were completely reversible over a complete cooling and heating cycle, indicating that the devices survive temperatures of 450 K and that the increase in current at higher temperature is not related to irreversible changes in junction structure. The Arrhenius plot of $\ln|J_{+0.2V}|$ versus $1000 T^{-1}$ shown in Figure 4B exhibits two linear regions, with a slope corresponding to 0.17 ± 0.1 meV for the 5–250 K region and 102.2 ± 8.0 meV for the 260–450 K region. Clearly, there is no significant thermal activation at temperatures below 100 K, but the apparent “activation barrier” of ~ 100 meV above 250 K deserves further comment.

The apparent “activation barrier” of 0.1 eV is too small to implicate solid state ion motion (typically 0.3–2 eV³³), is smaller than reported charge hopping conduction barriers³⁴ or *cis-trans* isomerization energies,³⁵ and is on the lower end of

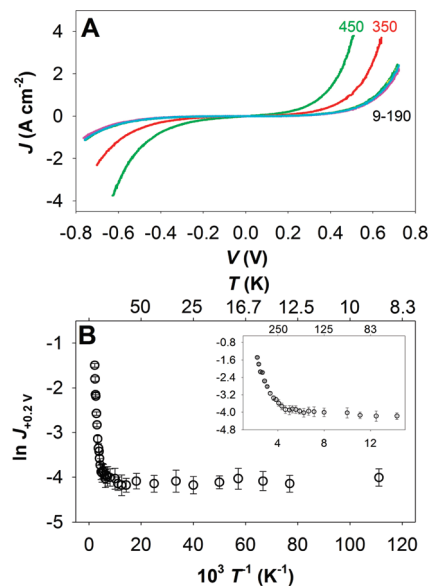


Figure 4. (A) Series of J - V curves for PPF/AB(3.2)/Cu junction for the temperature range 9–450 K. (B) Arrhenius plot for the data in (A). The inset in (B) shows an expanded view of the high temperature region. The apparent activation barriers calculated from this plot are 0.017 meV for the 9–250 K range and 100 meV for the high temperature (260–450 K) range.

expected phenyl ring rotation energies.¹¹ The temperature-dependent J - V characteristics were measured for several junctions containing various aromatic structures with thicknesses from 1.4–4.5 nm thick. In all cases, Arrhenius slopes are ≤ 0.1 eV for temperatures greater than ~ 250 K and much smaller for lower temperatures (see Table S-1 in the Supporting Information). These results imply that the charge transfer mechanism does not change in the range of thickness from 1.4 to 4.5 nm, and the temperature dependence is very similar for structurally distinct molecules. As shown below, the temperature dependence observed in the 250–450 K range is completely consistent with effects derived from the Fermi distribution of the electrons in the contacts and is not related to thermal activation of nuclear motion or structural rearrangements. This

important result indicates that reorganization, redox chemistry, ion motion, and so on, are not involved in electron transport in the temperature range considered here (5–450 K).

3.4. Analysis of Tunneling Transport. There are two common approaches for describing transport in molecular junctions. First, the mesoscopic physics community typically uses formulations rooted in the Landauer model for transport based on transmission probability.^{36–42} Second, the Simmons model for quantum mechanical tunneling is often applied to describe transport through molecular tunnel junctions.^{10,14,37,43–45} Because the experimental data are consistent with a tunneling mechanism, we will begin with the Simmons model⁴⁶ and adapt it for use in describing transport through molecules. For an in-depth description of the adaptation of the Simmons model to describe transport in molecular junctions, including the inherent limitations of the model in this context, the reader is directed elsewhere.⁴⁴

The simple expressions that describe tunneling through a rectangular barrier result in currents that are far too low to explain our results, and we must include the impact of image charge on the tunneling barrier shape to obtain reasonable agreement. Furthermore, the value of β we observe (2.5 nm⁻¹) is much smaller than values associated with nonresonant tunneling, which are typically in the range of 7–10 nm⁻¹ for alkanes and are associated with larger barrier heights.^{1,9,10,45,47,48} For example, a β of 8.8 nm⁻¹ was observed for PPF/diaminoalkane/Au junctions, structurally similar to those studied herein, but containing an aliphatic rather than aromatic molecule.⁴⁹ However, numerous measurements of β for aromatic systems in the range of 2–3 nm⁻¹ have been reported^{4,34,50,51} based both on molecular junctions and on electron transfer rates through aromatic monolayers in electrolyte solution.²⁹ Thus, an accurate model to describe transport in these molecular junctions must not only fit experimental J – V curves with reasonable accuracy but also explain the low value of the attenuation factor for aromatic systems in a self-consistent manner. In addition, any useful theory should provide at least a semiquantitative means to predict the electronic characteristics of molecular junctions as a function of molecular properties. As will be shown below, several parameters are important to determining the tunneling current, including (at least) the dielectric constant (ϵ) of the molecular layer, the tunneling barrier height (ϕ) and shape, and the effective carrier mass (m_e).

The simplified Simmons expression for the image charge-corrected current density (J) as a function of voltage (V) in a tunnel junction is^{46,52}

$$J = \frac{q}{2\pi h(\Delta s)^2} (\bar{\phi} e^{-A\sqrt{\bar{\phi}}} - (\bar{\phi} + qV) e^{-A\sqrt{\bar{\phi} + qV}}) \quad (1)$$

where q is the elementary charge (1.60 × 10⁻¹⁹ C), h is Planck's constant (6.63 × 10⁻³⁴ J s), Δs is the effective layer thickness (d_{eff} , described in more detail below) and

$$A = \left(\frac{4\pi\Delta s}{h} \right) \sqrt{2m_e} \quad (2)$$

where m_e is the effective carrier mass given as a fraction of the rest electron mass (9.11 × 10⁻³⁴ kg). In eq 1, the value of the barrier height ($\bar{\phi}$) is the average barrier value calculated from an expression that considers the full shape of the barrier taking image charge effects into account:

$$\bar{\phi} = \phi_0 - qV \left(\frac{s_2 + s_1}{2d} \right) - \left[1.15\lambda \frac{d}{s_2 - s_1} \right] \times \ln \left[\frac{s_2(d - s_1)}{s_1(d - s_2)} \right] \quad (3)$$

where ϕ_0 is the unmodified barrier height, d is the thickness of the barrier, s_i is the distance between the contact and the barrier at the Fermi level for each contact 1 and 2, and

$$\lambda = \frac{q^2 \ln 2}{8\pi\epsilon_0\epsilon d} \quad (4)$$

where ϵ_0 is the permittivity of free space and ϵ is the relative dielectric constant of the barrier layer. It can be shown from eq 3 that the net impact of including image charge is to round the corners of the rectangular barrier, reducing both the barrier height and the effective thickness of the barrier, with the magnitudes of ϕ_0 , ϵ , s_1 , and s_2 determining the value of $\bar{\phi}$ (although the value of m_e has a significant effect on the calculated value of J , as discussed below). The full barrier shape can be calculated through

$$\phi(x) = \phi_0 - qV \left(\frac{x}{d} \right) - 1.15\lambda \frac{d^2}{x(d-x)} \quad (5)$$

where x is any distance between the two contacts, ϕ_0 is the unmodified (rectangular) barrier height, and the ϕ axis is defined as originating at the Fermi energy level. Some examples of barrier shapes are presented below. It is important to note that eqs 1–4 are based on approximations due to considering only the most important (i.e., largest) terms in complex integrands given in the original Simmons derivations. A more detailed analysis that avoids these approximations has been presented recently (ref 36 and Supporting Information). The full model begins with the expression

$$J = c(\tilde{A} + \tilde{B} + \tilde{C}) \quad (6)$$

where

$$c = \frac{4\pi m_e q}{h^3} \quad (7)$$

and each term in the brackets is an integral in the original derivation. The solutions to the full integrands as given in ref 36 are

$$\tilde{A} = \frac{2qV}{A^2} \{ (A\sqrt{\bar{\phi}} + qV + 1) \exp(-A\sqrt{\bar{\phi} + qV}) - (A\sqrt{\eta + \bar{\phi}} + 1) \exp(-A\sqrt{\eta + \bar{\phi}}) \} \quad (8)$$

TABLE 1: Values for ϵ at 50 kHz for NAB Junctions and Calculated α for AB Oligomers

d (nm)	measured ϵ^a	molecule (d , nm)	α (\AA^3)
2.2	2.7	AB (1.12)	23.6
2.8	7.7	AB ₂ (2.2)	60.0
3.3	8.9	AB ₃ (3.2)	101.7
4.5	10.4	AB ₄ (4.3)	145.4
5.2	12.7	AB ₅ (5.3)	189.6

^a The value of ϵ is frequency dependent: for some examples, see Supporting Information, Figure S-4.

$$\tilde{B} = \frac{2}{A^2} \left\{ (A\sqrt{\bar{\phi}} + 1) \exp(-A\sqrt{\bar{\phi}}) - (A\sqrt{\bar{\phi}} + qV + 1) \times \exp(-A\sqrt{\bar{\phi}} + qV) \right\} \quad (9)$$

$$\tilde{C} = \frac{2}{A} \left\{ \left(\bar{\phi}^{3/2} + \frac{3}{A}\bar{\phi} + \frac{6}{A^2}\sqrt{\bar{\phi}} + \frac{6}{A^3} \right) \exp(-A\sqrt{\bar{\phi}}) - \left((\bar{\phi} + qV)^{3/2} + \frac{3}{A}(\bar{\phi} + qV) + \frac{6}{A^2}\sqrt{\bar{\phi} + qV} + \frac{6}{A^3} \right) \times \exp(-A\sqrt{\bar{\phi}} + qV) \right\} \quad (10)$$

where A is defined in eq 2, the other variables have been defined previously, and η is the Fermi level of the contact (taken as a positive value).

The effect of the approximation is most important for low barrier heights and thicknesses.³⁶ We will report here results based on both the approximate and full Simmons analysis to illustrate the effects of the commonly used approximations. Consider the error from the approximations to be the average of the % deviation of the $\ln J$ values obtained from the approximate eq 1 relative to the full model in eq 6 over the voltage range of ± 1 V. For a set of common parameters ($m_e = 1.0$, $s_1 = 0.05$ nm, $s_2 = d - s_1$, and $\epsilon = 5.0$), the error for $d = 2.2$ nm is 43% for $\phi = 1.0$ eV, 19% for $\phi = 5.0$ eV, and 11% for $\phi = 10.0$ eV. In addition, for $d = 5.2$ nm, the error is 26% for $\phi = 1.0$ eV, 5.5% for $\phi = 5.0$ eV, and 3.8% for $\phi = 10.0$ eV. Thus, although the error does become smaller for lower barrier values and thicker layers, it is still appropriate to apply the full model where possible.

Because the dielectric constant of the molecular layer has an effect on the image charge and the shape of the tunneling barrier in the Simmons model,⁴⁶ we evaluated the capacitance of the NAB junctions as a function of layer thickness to estimate values for ϵ (the relationships used to calculate ϵ from C are given in the Supporting Information, and Figure S-4 shows example J - V curves). Although ϵ is frequency dependent (Figure S-5), it increases significantly with thickness at all frequencies examined, as shown in Table 1 for 50 kHz. The values of 2.7–12.7 are consistent with dielectric constants for a variety of aromatic molecules, where values of 2.5 (biphenyl) to 35 (nitrobenzene) are typical for isolated molecules.⁵³ In a completed molecular junction, the absolute value of the dielectric constant depends on the structure of the molecular component and the nature of electronic coupling to the contacts and the measurement frequency.¹⁰ The impedance of the junction, which scales with device area and is frequency dependent, will determine the frequency range for which capacitance values can be obtained and therefore will also impact the measured value of ϵ . The accuracy of the values we obtain using this analysis relies on how well the junction corresponds to the simple capacitor that was used to model the current, which will depend on frequency

if there are parallel resistive and capacitive pathways in the molecular junction. For the NAB series, the junction area was large enough to result in reliable capacitance values at 50 kHz. For the AB series, the values of ϵ determined from a similar analysis could only be determined at a much higher frequency (200 kHz) because the junction areas were smaller, and therefore, the values of ϵ obtained were much smaller (see Figure S-5 in Supporting Information for an example and the literature¹⁰ for a discussion of junction area and measurements of ϵ). However, the measured values of ϵ for AB also increased significantly when increasing the thickness of the layer from 2.2 to 5.0 nm. In any case, a variation in ϵ with thickness is an indication of increased electron delocalization and greater polarizability for the thicker molecular layers. DFT calculation of the polarizability of a series of AB oligomers is shown in Table 1 and verifies that an increase in polarizability with molecular length is expected (and therefore the dielectric constant is also expected to increase as described through the Clausius–Mossotti relation⁵⁴). In addition, a recent theoretical paper⁵⁵ reports similar changes in polarizability and dielectric constant with thickness to those reported here. These observations are not surprising, given the conjugated nature of the component molecules, but have significant consequences in modeling tunneling transport. Effectively, as the molecular length increases, there is more delocalization of charge. This is supported by the visualizations of the molecular HOMO calculated using DFT, shown in the Supporting Information, Figures S-6 and S-7. In this case, the molecular HOMO extends across either an AB₂ unit (Figure S-6) or an AB₄ unit (Figure S-7). The fact that the HOMO still extends across the entire molecule for the latter case is one indication of why the polarizability and dielectric constant increase with molecular length. As shown by eqs 3–5 above, the value of ϵ modulates the barrier shape and overall average barrier that is used to calculate the tunnel current. In addition, an increase in the extent of conjugation can also have an impact on the molecular energy levels, which can possibly modify the barrier height as the thickness increases.

The tunneling barrier in a molecular device is often thought to correspond to the offset between the Fermi level (E_f) of the contact(s) and the molecular orbital energy (E_m) that lies closest in energy to E_f such that $\phi = E_f - E_m$. In most cases, the frontier orbitals are assumed to lie in closest proximity to the Fermi level and, therefore, are used to estimate ϕ . Aromatic molecules typically have HOMO levels of ~ -4.5 to -7 eV (relative to vacuum) and LUMO levels of -0.5 to -3 eV. The HOMO of NAB is estimated at -6.65 eV (DFT⁵⁶ B3LYP with 6-31(d) basis set) and is closest to the Fermi level of PPF (-4.90 eV⁵⁷), leading to a first approximation for the barrier height of 1.75 eV for hole transport through the HOMO. This approximation of the barrier height should be treated with caution, however, because it is known that molecular energy levels can undergo significant changes when brought into contact with the conductors in the molecular device.⁴² In addition, other effects may also become important, as discussed below. Because the molecular energies of aromatic structures are more closely aligned with the contact Fermi level than the corresponding orbital energies in aliphatic molecules, the estimated barrier heights for the aromatic molecular junctions reported herein are much lower. In addition, considerably different behavior as a function of length (e.g., the value of β) is expected due to the absence of conjugation in the aliphatic molecules.

Figure 5 shows plots of the barrier shape where $\phi_0 = 1.75$ eV (the dashed line in both plots) and $V = 0$. Figure 5A shows

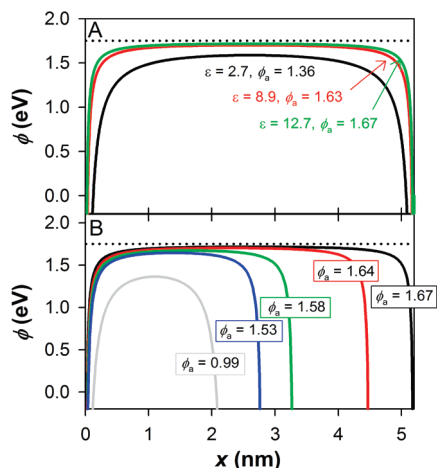


Figure 5. (A) Effect of the dielectric constant on the barrier shape for a 5.2 nm thick molecular layer with $\phi_0 = 1.75$ eV at zero bias. (B) Calculated barrier shapes for all five NAB layers using the values listed in Table 1 for ϵ .

the barrier shape predicted by eq 5 for three values of ϵ with a constant d (5.2 nm). ϕ_a is the average barrier height resulting from the shape calculation, while the values of s_1 and s_2 , which determine the effective layer thickness ($d_{\text{eff}} = \Delta s = s_2 - s_1$), are found from the x -axis intercepts of the plot. It is apparent that as the value of ϵ increases, the overall height of the barrier is larger, the corners become less rounded, and d_{eff} is larger. For example, when $\epsilon = 2.7$, the average barrier (ϕ_a) is 1.36 eV and the values for s_1 and s_2 are 0.125 and 5.0725 nm, respectively. Effectively, the average barrier height has been reduced by 0.39 eV and d_{eff} is reduced from 5.2 to 4.95 nm. However, if the value of ϵ is increased to 12.7, $\phi_a = 1.67$ and $d_{\text{eff}} = 5.15$ nm. These results illustrate that as the dielectric constant increases due to longer conjugation lengths, the barrier is less rounded and both ϕ_a and d_{eff} represent larger portions of ϕ_0 and d . Because ϵ increases with thickness, the changes in barrier shape and height should be incorporated into comparisons between theory and experiment. Figure 5B shows the full barrier shape calculations for the series of NAB thicknesses used to make the NAB devices of Figure 3B, using the experimentally determined values for ϵ . As shown, the average barrier height decreases from 1.67 eV for the 5.2 nm layer to 0.99 eV for the 2.2 nm layer. This decrease in barrier height is predicted only from considering the impact of an increasing ϵ on the barrier shape. However, if the value of ϕ_0 also varies with thickness, due to changes in the molecular HOMO energy, for example, the value of ϕ_a and the predicted tunneling current will be altered accordingly. Thus, it should be understood that the barrier shapes presented in Figure 5 illustrate how the image charge affects the barrier shape and average height. The actual barrier shape may be different because other effects may also contribute. However, Figure 5 does show how image charge effects can significantly alter a 1.75 eV barrier. The apparent barrier for an actual device can be estimated to a first-level by fitting the experimental data to the full Simmons model³⁶ in eqs 6–10 (of which eqs 1–4 are an approximate form) using the values of ϵ , ϕ_0 , and m_e as fitting parameters.

Figure 6 shows experimental J - V curves (open circles) for AB (A) and NAB (B) junctions as a function of thickness overlaid with the least-squares fits to the Simmons model (lines) using ϕ_0 , m_e , and ϵ as fit parameters (the error function was the sum of the square of the residual between the experimental and predicted $\ln J$ values). The fits were initiated with $m_e = 1$ and $\phi_0 = 1.75$ eV, and the experimental values for ϵ . In all cases,

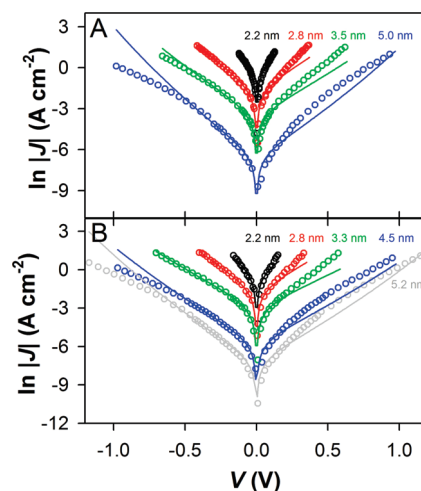


Figure 6. Fitting of experimental data (open circles) to the full Simmons model (lines) for AB (A) and NAB (B). The parameters obtained from a partial least-squares analysis using the approximation and the full model are given in Table 2.

TABLE 2: Parameters Obtained from Fitting Experimental Data to the Simmons Model, with Image Charge Effects Included^a

d (nm)	approximation (eqs 1–4)			full model (eqs 6–10) ³⁶		
	m_e	ϕ_0 (eV)	ϵ	m_e	ϕ_0 (eV)	ϵ
AB						
2.2	1.50	1.22	2.7	1.72	1.35	2.7
2.8	0.82	0.94	5.0	0.86	1.14	5.0
3.5	0.54	0.87	7.0	0.51	1.12	8.4
5.0	0.27	0.88	8.95	0.33	0.97	11.8
NAB						
2.2	1.48	1.25	2.7	1.47	1.46	2.7
2.8	0.80	1.04	4.0	0.84	1.25	4.0
3.3	0.48	0.995	8.9	0.49	1.26	9.3
4.5	0.30	0.970	10.4	0.33	1.16	10.6
5.2	0.24	0.967	12.7	0.27	1.07	14.8

^a The value of s_1 was fixed at 0.05 nm and s_2 was fixed at $d - s_1$ in all cases.

the fitted ϕ_0 and m_e values were accurate to ± 0.05 units, meaning that values outside this range yielded large errors. The semiempirical fits for the NAB dielectric constant in Table 2 agrees with those obtained from the capacitance (Table 1), with both exhibiting a significant increase with thickness. In addition, the average barrier height and effective carrier mass show significant changes with thickness for both AB and NAB. Because the values of ϕ_0 and m_e have a strong and interactive effect on the predicted J - V curves, it is important to analyze if the observed changes in either or both of these variables are physically reasonable.

It is known that HOMO and LUMO energies vary significantly as the length of conjugated oligomers is increased.^{30,37,47,50} Figure 7A shows a plot of DFT calculated HOMO (black curve) and LUMO (red curve) energies for azobenzene oligomers up to five units in length. As shown, the orbital energies change by ~ 0.5 eV with increasing length and conjugation. The work function of PPF and our Cu films have been measured,⁵⁷ yielding -4.9 and -4.7 eV, respectively. The average of these values is represented by the dashed line at -4.8 eV, illustrating that the frontier orbital energies move closer to E_f as length increases. Thus, the barrier height is calculated as the difference between E_f and E_{homo} since the molecular HOMO lies closer in energy to E_f . Indeed, as shown in Figure 7B, the barrier heights

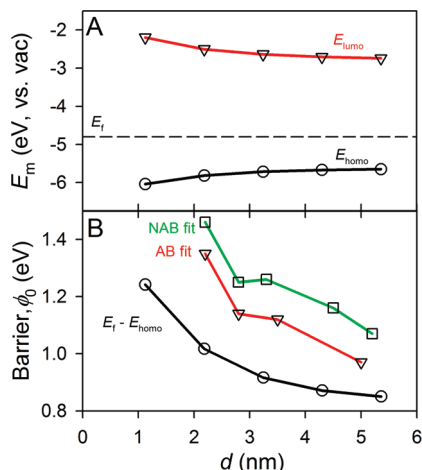


Figure 7. (A) Plot of the frontier orbital energies as a function of molecular length for a series of AB oligomers extending from the monomer to AB₄. (B) Plot of the tunneling barrier vs thickness determined from the calculations ($E_i - E_{homo}$ for $E_i = -4.8$ eV) and for fitting of experimental data to the full Simmons model.

predicted from DFT decrease with increasing length (black curve). In addition, the values obtained from the least-squares analysis above correlate well with this trend for both AB (red curve) and NAB (green curve). This calculation has also been performed for other oligomeric species of conjugated structures, as shown in the Supporting Information (Figure S-8). In all cases, the increase in conjugation and electron delocalization with length significantly changes the HOMO energy and predicted barrier height. A consequence of a barrier height which varies with thickness is that the attenuation factor, β , does not reflect a single barrier height, but also includes its variation with thickness. It should also be noted that eqs 1–4 do not accurately predict the effect of thickness on the J – V response with a single barrier height of any physically reasonable value and results in a β value significantly larger than that observed experimentally. For example, setting ϕ_0 to 0.3 eV and $m_e = 1.0$ predicts a β of 6.7 nm^{-1} , using the experimental dielectric constants.

Although Figure 7 and the least-squares analysis indicate that the value of ϕ_0 varies with thickness, fitting of the experimental data also produced a variation in m_e . It is known that the effective mass (defined as m/m_0) of tunneling electrons (or holes) can vary from unity due to a variety of factors. For example, Joachim and Magoga⁵⁸ predicted that changes in m_e could produce β values in the range of 1 – 4 nm^{-1} for conjugated systems and calculated an m_e of 0.163 for the case of a polyphenylene molecular layer. Moreover, they showed that the value of m_e can depend on energy. In addition, other relationships between the effective mass and tunneling distance have been proposed.⁵⁹ Variations in effective mass are clearly possible as the molecular layer thickness increases. This can be understood by considering that the effective mass of an electron is expected to decrease as delocalization increases due to changes in the dispersion relationship for the molecular layer. The measured and calculated increases in dielectric constant and polarizability with length confirm this expectation. It is important to note that the decrease in m_e with molecular length indicates that extensive conjugation can result in charge carriers that behave as light particles having only a fraction of the mass of an electron. This implies that highly conjugated systems may be expected to show much less dependence of current on the tunneling distance, resulting in smaller β values, and that molecules could be engineered to have very small effective mass values to result in efficient tunneling. The extremely low β

values recently reported for a variety of highly conjugated structures are consistent with this supposition.⁶⁰ Although it is becoming apparent that the values of ϵ , m_e , and ϕ_0 are not independent variables, as assumed in the mathematical treatment outlined above, it is not clear exactly how these variables are related for the case of a molecular tunneling junction. Thus, it is currently not possible to predict, for example, how a change in dielectric constant impacts the value of the tunneling barrier height and the effective carrier mass or how to relate these parameters quantitatively to molecular structure. Such insights would permit design of particular molecular structures for targeted electronic functions, enabling the design of complex and novel devices through chemical synthesis. We are currently working toward a more detailed understanding of the interplay between effective mass, barrier height, and molecular structure.

While the fits to experimental curves (Figure 6) and the results shown in Figure 7 indicate that ϵ , ϕ_0 , and m_e vary with molecular layer thickness, other variables may also play a role in determining the tunneling current in these junctions. For example, a distribution of molecular energy levels due to homogeneous and inhomogeneous broadening certainly exists in the large area junctions considered in this work. The value of the barrier height therefore may actually represent an average that includes a number of states with a lower barrier than the overall average. Because the barrier height is in the range of 0.8–1.25 eV, there may actually be a subset of resonant transport channels with energies close or equal to the contact Fermi level (see discussion below). In addition, electronic coupling to the contacts and intermolecular interactions may play a significant role in determining the barrier shape and height. In effect, the extracted transport parameters obtained from fitting experimental data to the Simmons model must be considered in the context of a possibly wide range of phenomena.

3.5. Dependence of the Tunnel Current on Temperature.

As shown above, the Simmons model can be used to obtain reasonable correspondence to our experimental data and is consistent with the shapes of the J – V curves, the exponential thickness dependence, and the temperature independent conductance regime that extends from 5 to ~ 200 K, provided changes in molecular energy levels and effective mass with length are taken into account. We now consider if the apparent “activation” of conduction for temperatures exceeding ~ 200 K is consistent with a tunneling mechanism or if the transition represents a change in transport mechanism at elevated temperatures. Simmons⁶¹ showed that a significant increase in tunneling current can result due to redistribution of electrons around the Fermi level of the contacts. We have used this approach to calculate the expected current as a function of temperature. In this formulation, the effect of image charge is ignored in order to simplify the analysis. Figure 8 shows an overlay of Arrhenius plots for experimental data and the theoretically predicted temperature dependence for several combinations of ϕ_0 and m_e . First, for (a), $\phi_0 = 0.58$ and $m_e = 0.9$, the predicted current is larger than that experimentally observed (open circles), but the shape of the Arrhenius plot is qualitatively reproduced. Predicted Arrhenius slopes in this case are 0.12 meV for the low temperature region (5–245 K) and 64 meV for higher temperatures (290–450 K). Next, for case (b), $\phi_0 = 0.58$ and $m_e = 1.1$, the overall shape is accurately predicted and the calculated apparent activation barriers are 0.15 and 92 meV for the low and high temperature regions, respectively. Finally, for case (c), $\phi_0 = 0.9$ and $m_e = 0.65$, a lower current is predicted, but again the shape is qualitatively reproduced, yielding calculated apparent activation barriers of

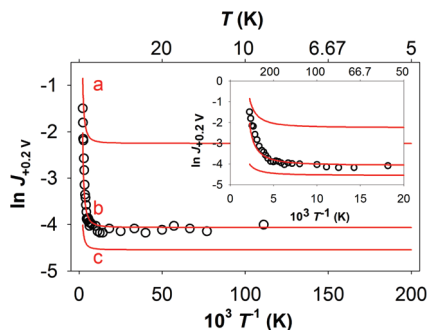


Figure 8. Overlay of Arrhenius plots for experimental data ($\ln J_{0.2V}$ vs $1000/T$ for a PPF/AB(3.2)/Cu junction) and those obtained from the Simmons relationship that includes the effect of temperature on the distribution of electrons around the Fermi level.⁶¹ Points are experimental, with lines calculated for the Simmons model with (a) $\phi_0 = 0.58$ eV, $m_e = 0.9$; (b) $\phi_0 = 0.58$ eV, $m_e = 1.1$; (c) $\phi_0 = 0.9$, $m_e = 0.65$. Inset is an expanded view.

0.05 and 23 meV (low and high T , respectively). The values of ϕ_0 and m_e used in Figure 8 cannot be compared directly to those in Table 2 because the image charge is neglected in the temperature analysis. However, the qualitative similarity of predicted and observed Arrhenius plots and the quantitative agreement of the Arrhenius slopes of several different molecules and thicknesses (see Supporting Information, Table S-1) for high (35–102 meV) and low T (0.02–0.3 meV) indicate that the observed temperature dependence is consistent with a tunneling mechanism, with no thermal activation of the molecular layer involved. The increase in current density for $T > 250$ K is a result of the presence of electrons (or holes) at energies above (or below) the Fermi energy of the contacts. The agreement with Simmons predictions (Figure 8) and the fact that the Arrhenius slopes are too small to be associated with reasonable molecular restructuring or ion motion lead to the conclusion that no molecular reorganization, redox reaction, or conformational changes are required to generate the observed temperature dependence. A similar effect has been reported to account for the temperature dependent current in nanogap molecular junctions using a molecular level model based on the Landauer formula.⁶² Thus, the Fermi function can be used to explain the type of temperature dependence we observe experimentally regardless of the specific model used, further indicating that it is a plausible explanation.

3.6. Consequences of Tunneling through Aromatic Structures. Although quantum mechanical tunneling appears to describe transport in carbon/molecule/Cu junctions, there are several points which deserve additional discussion. First, the value for β of 2.5 nm^{-1} is much smaller than values typically associated with nonresonant tunneling and indicates that tunneling can produce substantial currents across relatively thick molecular junctions (i.e., 5 nm). Second, although tunneling across 2–5 nm is possible with tunneling barriers in the 0.5–1.5 eV range, the existence of resonant transport channels cannot be excluded. The expected distribution of molecular energy levels from the larger number of molecules ($>10^{10}$) in each junction could give rise to a subset of very low tunneling barrier values that may also impact the overall current. In this case, the competition between the tunneling and resonant current channels would determine the overall current measured experimentally, and the characteristics that correspond to the expectations for nonresonant tunneling may still be observed if the nonresonant current represents the majority. Finally, when the value of the (average) barrier decreases past some critical level,

the resonant current should become dominant, as discussed recently for aromatic molecules in STM break junctions.⁶³

Collectively, the results in this paper indicate that robust and reproducible junctions can be fabricated in high yield and that nonresonant tunneling is likely to be the transport mechanism. Importantly, the result that dielectric constant (experimentally measured), barrier height, and effective mass (determined from calculations and fitting of data) change with thickness provides powerful evidence that transport occurs via through-bond rather than through-space tunneling, because a change in the structure of the molecular component underlies the variation in ϵ , ϕ_a , and m_e with thickness. In addition, the temperature dependence of the current is completely consistent with variation of electron distribution by the Fermi function, rather than any “activated” process. Taken together, the effect of structure on the electronic properties of the junctions along with the lack of any molecular activation provides compelling evidence that an array of short circuit filaments cannot give rise to the electronic response of the system. Although the molecular layers employed in this approach are more disordered and often contain multilayers (as compared to those based on self-assembled monolayers), their irreversible bonding prevents restructuring and metal filament formation. The robust nature of diazonium-derived molecular layers enables a highly reproducible method for making molecular junctions by vapor deposition for both systematic studies of charge transport mechanisms and possibly for practical applications. Although the present results strongly argue against metal filament formation, “partial” filaments resulting from metal penetration to form localized tunnel gaps are harder to rule out. They would have to be very reproducible themselves to yield the observed low standard deviations of current densities, which is unlikely for random formation of “hot spots”. Furthermore, we reported recently using a very different metal deposition technique based on “cold” metal diffusion that both indirect and direct deposition of Cu yielded quantitatively similar J – V curves.⁴⁹

4. Conclusions

Molecular junctions fabricated by covalent bonding of aromatic molecular layers to carbon electrodes with evaporated Cu top contacts can be made with high yield, are highly reproducible, and robust to potential cycling and elevated temperatures (at least 180 °C). Analysis of the thickness and temperature dependence of J – V curves for junctions containing multilayer films of nitroazobenzene and azobenzene indicate that charge transport occurs through a tunneling mechanism over a range of thicknesses extending up to 5.2 nm and temperatures from 5 to 450 K. The Simmons relationship that includes the effect of temperature on the distribution of charge carriers in the contacts shows that no thermal activation is necessary to explain our results over a wide range in temperature, despite the appearance of an activated region in experimental Arrhenius plots. Instead, the increase in J at elevated temperatures observed experimentally arises solely from the temperature dependence of the contact Fermi function(s). Parameters derived from analysis of experimental data in light of the Simmons model (including the effects of image charge) indicate that the barrier height and/or shape, effective carrier mass, and the dielectric constant of the molecular layer change as thickness increases. These findings are supported by experimental data, DFT calculations, and theoretical models outlined in the literature. The way in which these parameters change with thickness determines the value of the attenuation factor measured for a particular aromatic system, providing a possible origin of the

range of values reported for aromatic molecules. Finally, the barrier height is quite small compared to reported values for nonaromatic molecular junctions, indicating that for the junctions studied here, the effect of resonant transport channels may become important.

Acknowledgment. This work was supported by Natural Sciences and Engineering Research Council of Canada, the National Institute for Nanotechnology, The University of Alberta, and The MicroSystems Technology Research Initiative. The National Institute for Nanotechnology is operated as a partnership between the National Research Council and the University of Alberta and is jointly funded by the Government of Canada, the Government of Alberta, and the University of Alberta. We thank Amr M. Mahmoud for help with several measurements, and Professor S. Jiménez Sandoval, Haijun Yan, and Nikola Pekas for valuable discussions. Finally, we thank a reviewer for bringing the full Simmons model (eqs 6–10) to our attention and for other valuable comments.

Supporting Information Available: Supplemental figures, equations, and tables are available. This material is available free of charge via the Internet at <http://pubs.acs.org>.

References and Notes

- Akkerman, H. B.; de Boer, B. *J. Phys.: Condens. Matter* **2008**, *20*, 013001.
- Chen, F.; Hihath, J.; Huang, Z. F.; Li, X. L.; Tao, N. *J. Annu. Rev. Phys. Chem.* **2007**, *58*, 535–564.
- McCreery, R. L. *Chem. Mater.* **2004**, *16*, 4477–4496.
- McCreery, R. L.; Bergren, A. *J. Adv. Mater.* **2009**, *21*, 4303–4322.
- Metzger, R. M. *Chem. Rev.* **2003**, *103*, 3803.
- Selzer, Y.; Allara, D. *Annu. Rev. Phys. Chem.* **2006**, *57*, 593–623.
- Ulgut, B.; Abruna, H. D. *Chem. Rev.* **2008**, *108*, 2721–2736.
- Vilan, A.; Yaffe, O.; Biller, A.; Salomon, A.; Kahn, A.; Cahen, D. *Adv. Mater.* **2010**, *22*, 140–159.
- Akkerman, H. B.; Blom, P. W. M.; de Leeuw, D. M.; de Boer, B. *Nature* **2006**, *441*, 69–72.
- Akkerman, H. B.; Naber, R. C. G.; Jongbloed, B.; van Hal, P. A.; Blom, P. W. M.; de Leeuw, D. M.; de Boer, B. *Proc. Natl. Acad. Sci. U.S.A.* **2007**, *104*, 11161–11166.
- Anariba, F.; McCreery, R. L. *J. Phys. Chem. B* **2002**, *106*, 10355–10362.
- Anariba, F.; Steach, J. K.; McCreery, R. L. *J. Phys. Chem. B* **2005**, *109*, 11163–11172.
- Bergren, A. J.; Harris, K. D.; Deng, F. J.; McCreery, R. L. *J. Phys.: Condens. Matter* **2008**, *20*, 374117.
- DiBenedetto, S. A.; Facchetti, A.; Ratner, M. A.; Marks, T. J. *J. Am. Chem. Soc.* **2009**, *131*, 7158–7168.
- Scott, A.; Janes, D. B.; Risko, C.; Ratner, M. A. *Appl. Phys. Lett.* **2007**, *91*, 033508.
- McCreery, R. L.; Wu, J.; Kalakodimi, R. P. *Phys. Chem. Chem. Phys.* **2006**, *8*, 2572–2590.
- Anariba, F.; DuVall, S. H.; McCreery, R. L. *Anal. Chem.* **2003**, *75*, 3837–3844.
- Nowak, A. M.; McCreery, R. L. *Anal. Chem.* **2004**, *76*, 1089–1097.
- Nowak, A. M.; McCreery, R. L. *J. Am. Chem. Soc.* **2004**, *126*, 16621–16631.
- Anariba, F.; Viswanathan, U.; Bocian, D. F.; McCreery, R. L. *Anal. Chem.* **2006**, *78*, 3104–3112.
- Bonifas, A. P.; McCreery, R. L. *Chem. Mater.* **2008**, *20*, 3849–3856.
- Mahmoud, A. M.; Bergren, A. J.; McCreery, R. L. *Anal. Chem.* **2009**, *81*, 6972–6980.
- Kariuki, J. K.; McDermott, M. T. *Langmuir* **1999**, *15*, 6534–6540.
- Kariuki, J. K.; McDermott, M. T. *Langmuir* **2001**, *17*, 5947–5951.
- Pinson, J.; Podvorica, F. *Chem. Soc. Rev.* **2005**, *34*, 429–439.
- Ranganathan, S.; McCreery, R.; Majji, S. M.; Madou, M. J. *Electrochem. Soc.* **2000**, *147*, 277–282.
- Solak, A. O.; Eichorst, L. R.; Clark, W. J.; McCreery, R. L. *Anal. Chem.* **2003**, *75*, 296–305.
- McGovern, W. R.; Anariba, F.; McCreery, R. L. *J. Electrochem. Soc.* **2005**, *152*, E176–E183.
- Yang, H.-H.; McCreery, R. L. *Anal. Chem.* **1999**, *71*, 4081–4087.
- Liu, H. M.; Wang, N.; Zhao, J. W.; Guo, Y.; Yin, X.; Boey, F. Y. C.; Zhang, H. *ChemPhysChem* **2008**, *9*, 1416–1424.
- Engelkes, V. B.; Beebe, J. M.; Frisbie, C. D. *J. Am. Chem. Soc.* **2004**, *126*, 14287–14296.
- Chen, F.; Li, X. L.; Hihath, J.; Huang, Z. F.; Tao, N. *J. Am. Chem. Soc.* **2006**, *128*, 15874–15881.
- Mujica, V.; Malaver, M.; Ruelle, F. *J. Phys. Chem. A* **1999**, *103*, 89–94.
- Choi, S. H.; Kim, B.; Frisbie, C. D. *Science* **2008**, *320*, 1482–1486.
- Conti, I.; Garavelli, M.; Orlandi, G. *J. Am. Chem. Soc.* **2008**, *130*, 5216–5230.
- Huisman, E. H.; Guedon, C. M.; van Wees, B. J.; van der Molen, S. J. *Nano Lett.* **2009**, *9*, 3909–3913.
- Malen, J. A.; Doak, P.; Baheti, K.; Tilley, T. D.; Segalman, R. A.; Majumdar, A. *Nano Lett.* **2009**, *9*, 1164–1169.
- Moth-Poulsen, K.; Bjornholm, T. *Nat. Nanotechnol.* **2009**, *4*, 551–556.
- Paulsson, M.; Datta, S. *Phys. Rev. B* **2003**, *67*, 241403.
- Samanta, M. P.; Tian, W.; Datta, S.; Henderson, J. I.; Kubiak, C. P. *Phys. Rev. B* **1996**, *53*, R7626–R7629.
- Thijssen, J. M.; Van der Zant, H. S. J. *Phys. Status Solidi B* **2008**, *245*, 1455–1470.
- Thygesen, K. S.; Rubio, A. *Phys. Rev. Lett.* **2009**, *102*, 046802.
- Salomon, A.; Boecking, T.; Seitz, O.; Markus, T.; Amy, F.; Chan, C.; Zhao, W.; Cahen, D.; Kahn, A. *Adv. Mater.* **2007**, *19*, 445–450.
- Vilan, A. *J. Phys. Chem. C* **2007**, *111*, 4431–4444.
- Wang, W. Y.; Lee, T.; Reed, M. A. *Phys. Rev. B* **2003**, *68*, 035416.
- Simmons, J. G. *J. Appl. Phys.* **1963**, *34*, 1793–1803.
- Beebe, J. M.; Kim, B.; Frisbie, C. D.; Kushmerick, J. G. *ACS Nano* **2008**, *2*, 827–832.
- Beebe, J. M.; Kim, B.; Gadzuk, J. W.; Frisbie, C. D.; Kushmerick, J. G. *Phys. Rev. Lett.* **2006**, *97*, 026801.
- Bonifas, A. P.; McCreery, R. L. *Nat. Nanotechnol.* **2010**, *5*, 612–617.
- Choi, S. H.; Risko, C.; Delgado, M. C. R.; Kim, B.; Bredas, J.-L.; Frisbie, C. D. *J. Am. Chem. Soc.* **2010**, *132*, 4358–4368.
- Salomon, A.; Cahen, D.; Lindsay, S.; Tomfohr, J.; Engelkes, V. B.; Frisbie, C. D. *Adv. Mater.* **2003**, *15*, 1881–1890.
- Simmons, J. G. *J. Appl. Phys.* **1963**, *34*, 2581–2590.
- CRC Handbook of Chemistry and Physics*, 76th ed.; Lide, D. R., Ed.; CRC Press: New York, 1996.
- Younglove, B. A. *J. Chem. Phys.* **1968**, *48*, 4181–4186.
- Natan, A.; Kuritz, N.; Kronik, L. *Adv. Funct. Mater.* **2010**, *20*, 2077–2084.
- Frisch, M. J.; Trucks, G. W.; Schlegel, H. B.; Scuseria, G. E.; Robb, M. A.; Cheeseman, J. R.; Montgomery, J. A.; Vreven, T.; Kudin, K. N.; Burant, J. C.; Millam, J. M.; Iyengar, S. S.; Tomasi, J.; Barone, V.; Mennucci, B.; Cossi, M.; Scalmani, G.; Rega, N.; Petersson, G. A.; Nakatsuji, H.; Hada, M.; Ehara, M.; Toyota, K.; Fukuda, R.; Hasegawa, J.; Ishida, M.; Nakajima, T.; Honda, Y.; Kitao, O.; Nakai, H.; Klene, M.; Li, X.; Knox, J. E.; Hratchian, H. P.; Cross, J. B.; Bakken, V.; Adamo, C.; Jaramillo, J.; Gomperts, R.; Stratmann, R. E.; Yazyev, O.; Austin, A. J.; Cammi, R.; Pomelli, C.; Ochterski, J. W.; Ayala, P. Y.; Morokuma, K.; Voth, G. A.; Salvador, P.; Dannenberg, J. J.; Zakrzewski, V. G.; Dapprich, S.; Daniels, A. D.; Strain, M. C.; Farkas, O.; Malick, D. K.; Rabuck, A. D.; Raghavachari, K.; Foresman, J. B.; Ortiz, J. V.; Cui, Q.; Baboul, A. G.; Clifford, S.; Cioslowski, J.; Stefanov, B. B.; Liu, G.; Liashenko, A.; Piskorz, P.; Komaromi, I.; Martin, R. L.; Fox, D. J.; Keith, T.; Al-Laham, M. A.; Peng, C. Y.; Nanayakkara, A.; Challacombe, M.; Gill, P. M. W.; Johnson, B.; Chen, W.; Wong, M. W.; Gonzalez, C.; Pople, J. A. *Gaussian 03*, 6.0 ed.; Gaussian, Inc.: Pittsburgh, 2004.
- Yan, H.; McCreery, R. L. *ACS Appl. Mater. Interfaces* **2009**, *1*, 443–451.
- Joachim, C.; Magoga, M. *Chem. Phys.* **2002**, *281*, 347–352.
- Tomfohr, J. K.; Sankey, O. F. *Phys. Rev. B* **2002**, *65*, 245105.
- Sedghi, G.; Sawada, K.; Esdaile, L. J.; Hoffmann, M.; Anderson, H. L.; Bethell, D.; Haiss, W.; Higgins, S. J.; Nichols, R. J. *J. Am. Chem. Soc.* **2008**, *130*, 8582–8583.
- Simmons, J. G. *J. Appl. Phys.* **1964**, *35*, 2655–2658.
- Poot, M.; Osorio, E.; O'Neill, K.; Thijssen, J. M.; Vanmaekelbergh, D.; van Walree, C. A.; Jenneskens, L. W.; van der Zant, H. S. J. *Nano Lett.* **2006**, *6*, 1031–1035.
- Xing, Y. J.; Park, T.-H.; Venkatramani, R.; Keinan, S.; Beratan, D. N.; Therien, M. J.; Borguet, E. *J. Am. Chem. Soc.* **2010**, *132*, 7946–7956.